Acoustic and Thermoacoustic Jet Propulsion

J. Schoenmaker[1†], D. A. Machado[2], H. Frandini[3], A. Hetem Junior[1] and F. A. S. Mota[1]

[1] *Center for Engineering, Modeling and Applied Social Sciences, Federal University of ABC, Av. dos Estados 5001, bairro Bangú, Santo André, SP CEP 09210-580 Brazil*

[2] *Combustion and Propulsion Laboratory, National Institute for Space Research, Rodovia Presidente Dutra, km 40, Cachoeira Paulista, SP, CEP 12630-970, Brazil*

[3] *Center for Natural and Human Sciences, Federal University of ABC, Av. dos Estados 5001, bairro Bangú, Santo André, SP CEP 09210-580 Brazil (Current address: SBND Laboratory, Neutrino Division – Fermilab – Batavia, IL 60510 USA)*

†*Corresponding Author Email: jeroen.schoenmaker@ufabc.edu.br*

ABSTRACT

This manuscript bridges the fields of jet propulsion, synthetic jets and thermoacoustic engines. We introduce the case that synthetic jets in air can be considered a consistent approach for propulsion systems. To date, studies on synthetic jet propulsion have been scattered and rather subsidiary. Furthermore, investigating the perspective of propulsion can provide new insights into the field of synthetic jets and the physics of propulsion. In this work, synthetic jet propulsion in air is demonstrated and studied for acoustic and thermoacoustic cases. We developed synthetic jet systems and characterized the resulting propulsion regarding several relevant parameters such as geometric factors and the frequency and power of acoustic jets electromechanically and thermally produced. We demonstrated the 10.4-mN and 2.7-mN thrust in the acoustic and thermoacoustic modes, respectively, using compact tabletop assemblies. The physical mechanism of the jets has been modeled, simulated, verified with Schlieren imaging and laid in the perspective of adherent literature. Similarities and differences regarding traditional jet propulsion systems are discussed. Synthetic jet propulsion in air using a thermal cycle is experimentally demonstrated for the first time.

NOMENCLATURE

A	area of the jet flow	r	ring flow radius
a	radius of vortex disc	T	thrust
b	distance between 1st and 2nd screens	U	translational velocity of vortex ring
D	nozzle exit diameter	V	amplitude of applied voltage
D1	1st screen orifice diameter	v	velocity of the jet stream
D2	2nd screen orifice diameter	x	direction of flow
E'	normalized kinetic energy	Γ	circulation – defined by Eq.11
F	frequency of applied voltage	α	nozzle tapering angle
I	hydrodynamic impulse	δ	Dirac delta function
L	nozzle neck length	κ	vortex filament of strength
m	mass	λ	radius ratio defined by Eq. 6
P	power	μ	fluid viscosity
p	pressure	ρ	fluid density
R	vortex ring radius	τ	temperature
$\bar{R}$	ideal gas constant	ω	angular frequency of the driving voltage

1. INTRODUCTION

Great relevance has been given to the development of alternative engine solutions that are efficient, reliable and mechanically simple (Backhaus and Swift 1999). For alternative nonconventional propulsion systems, a change in perspective can draw considerable attention (Xu *et al*. 2018).

In 1950, Ingård and Labate (1950) published a manuscript that investigated acoustic streaming phenomena around orifices. Their setup was akin to the acoustic apparatus that we have built for this work, although they did not aim for propulsion applications. Instead, their investigation focused on the nature of the jets formed in such conditions. While addressing the velocity of the stream, they measured a maximum thrust of 1,37 mN in their system, which was the first systematic registry of synthetic air jet thrust known by the authors of this work. In his 2008 book "Notes on Acoustics", Ingård returned to the subject and dedicated a subsection to acoustic propulsion. A well-known physics class demonstration was presented, where a small thrust was observed in Helmholtz resonators comprised of Christmas tree spherical ornaments. The phenomenon is described as an "amusing and perhaps puzzling" demonstration whose details and mathematical model remain challenging (Ingard 2008).

Presently, the field of synthetic jet research is established, advances the overall comprehension of the phenomena involved (Glezer and Amitay 2002, Holman *et al.* 2005, Trávníček *et al.* 2012, Jankee and Ganapathisubramani 2019) and settles applications, which are mainly adherent to flow control (Pack and Seifert 2001, McCormick 2000, Crowther and Gomes 2008), attitude control and assistance for aircrafts (Li and Yang 2017) and micro air vehicles (Whitehead and Gursul 2006), heat transfer (Jeng and Hsu 2016) and mixing (Wang and Menon 2001).

From the literature, we highlight a number of works that are more adherent to the concept of a resulting force generated by synthetic jets, which will be addressed in more detail in the manuscript. Interestingly, bioinspired by sea creatures such as squids and salps, a propulsion system has been proposed for small water vehicles using jets produced by speaker coils as actuators (Thomas *et al.* 2005, Dabiri 2009, Qin *et al.* 2020). Paxson *et al.* used synthetic jets produced by loudspeakers to investigate thrust augmentation for pulse detonation-based propulsion systems (Paxson *et al.* 2007). To establish a new practical experimental procedure for evaluating the efficiency of synthetic jets, Gil and Smyk (2019) characterized the reaction force produced by loudspeaker actuators. Last, Kordík and Trávníček (2018) tested nozzle shapes to enhance the jet momentum flux in synthetic jet actuators.

We note that current research on synthetic jets for the purpose of propulsion is mostly focused on underwater applications. In this work, we focus on aerial environments. Furthermore, synthetic jet research largely relies on electromechanical transducers, since jets are typically generated by speaker coils, piezoelectric actuators and pistons. This work aims to put forward the study of acoustic jets that are mechanically and thermally produced. In this sense, it is appropriate to bring attention to another synthetic jet propulsion system that is not traditionally recognized as such. In 1891, Thomas Piot filed a patent for a steam engine that would be responsible for propelling a toy known as a pop pop boat (Piot 1892). It is a candle-fed steam engine with no movable parts that generates a steam cycle, which forms pulsed water jets that propel a small boat (Dobson 2003). From the fundamental physics perspective, the thermoacoustic jet engines in this work can be considered the Stirling version of the pop pop boat engine. To our knowledge, only one study investigating synthetic jets driven by a thermoacoustic engine has been published (Chen *et al.* 2020). Although this represents a bold step toward the thermal realm, this study does not focus on propulsion and presents results that are restricted to numerical simulations.

Thermoacoustic engines are known for being highly efficient and mechanically simple and possibly assembled with no moving parts (Swift 1988); thus, they are strong candidates for reliable and sustainable applications. In the context of this manuscript, the only thermoacoustic air jet propulsion proposal that we know of is the recent system crafted by an independent developer based on a horizontal version of the Rijke tube (Blade 2021); this system is concomitant to our project.

What if the efficiency of Stirling engines can be harnessed in terms of jet propulsion by synthetic jets? To address this question, we divided the project into two separate inquiries: one regarding the consistency of synthetic jets in terms of propulsion and the other whether it is possible to attain sustained and consistent propulsion from a thermoacoustic engine. In the current propulsion systems paradigm, acoustic phenomena should be avoided, since they are considered deleterious for optimal performance in most cases. In this work, we inverse the argument and assess how acoustic motion can be used in favor of propulsion.

As a final remark, vortex rings are key elements for distinct research areas such as synthetic jets, pulsed jets and pulsejet propulsion. Beyond the first glance similarities, synthetic jets are essentially distinct from the other aforementioned areas in several important aspects (Chang *et al.* 2020). A synthetic jet results from a continuous and reciprocating motion (often generated by actuators such as pistons, piezo drivers, loudspeakers, but not necessarily so), where a series of vortex rings is formed outside the nozzle, while the net mass flow through the nozzle is essentially zero. A pulse jet (also known as a free jet or underexpanded turbulent jet) results from a disturbance of a static environment. This type of jet appears when a high-pressure gas is suddenly released into a low-pressure gas through a nozzle (Chitsaz *et al.* 2011). Pressure ratios are usually well above unity, and expansion velocities are described in terms of Mach numbers (often supersonic), so they are orders of magnitude higher than the pressures and propagation rates measured in this work, which are approximately 10^{-4} and Mach ~0.02, respectively (Ishii *et al.* 1999). Finally, the pulsejet is an established propulsion technology that has been used since the beginning of the last century. Devices based on this technology operate far from the conditions described for synthetic jets and are often an internal combustion jet engine with a nonzero net flow rate (Geng *et al.* 2010). In this work, we introduce the

case of a propulsion system based on synthetic jets that are mechanically and thermally produced in air.

2. ACOUSTIC JETS

2.1 Acoustic Propulsion Measurements

To address the propulsion properties of synthetic jets, we investigated the resulting propulsion of jets produced through a 10-cm-diameter loudspeaker (20-W max nominal power; 4-Ω impedance). A tapering nozzle was attached to the loudspeaker, which was driven by a sinusoidal voltage produced by a function generator with fine control of frequency and amplitude. Similar to the work of Ingård and Labate (1950), the thrust of the jet was measured by the force exerted on a screen placed in the jet stream (Fig. 1). In some measurements, a 5-cm-long cylindrical cavity was placed between the loudspeaker and the tapering nozzle.

In Fig. 2, we show the results of the thrust (T) as a function of the frequency of the driving voltage (F) for four different voltage amplitudes (V). The four curves present similar asymmetric and very regular thrust distributions with a maximum at approximately $F = 70$ Hz. The cylindrical cavity was present in this series of measurements, and the nozzle exit diameter was D = 21 mm with length L = 15 mm. This distribution can be essentially understood as a result of the counterbalance between fostering and suppressing thrust agents. At lower frequencies, each pulse contributes by summing up to the overall thrust, so increasing frequency results in higher propulsion. However, when the frequency becomes sufficiently high, suppressing factors, such as compressive fluid dampening and electromechanical response of the transducer, play a significant role. The overall thrust distribution in frequency is consistent with the results reported by Gil and Smyk (2019), and important factors that determine this distribution are discussed in Section 2.4. Throughout the remainder of this manuscript, we explore many relevant parameters that influence the thrust yield of this type of system; now, we would like to discuss the basic aspects of jet propulsion.

Considering a conventional jet propulsion system operating in ideal conditions, we can model the thrust

(T), power (P) and air flow by equations 1, 2 and 3, respectively:

$$T = \frac{dm}{dt}v \tag{1}$$

$$P = \frac{1}{2}\frac{dm}{dt}v^2 \tag{2}$$

$$\frac{dm}{dt} = \rho A v \tag{3}$$

where m is the mass, v is the velocity of the flow at the nozzle, A is the transversal area of the nozzle, and ρ is the density of the medium. Combining the equations, one can obtain

$$P^2 = \frac{T^3}{4\rho A} \tag{4}$$

from which we apprehend the general correlation $P^2 \propto T^3$ of jet propulsion systems.

In our setup, we use a loudspeaker to produce synthetic jets using electric power. Typically, loudspeakers yield approximately 1% of the electric power in sound pressure. It is reasonable to assume that the produced sound pressure is proportional to the electric power input to the loudspeaker, and the power of the system is given by $P = V^2/Z$, where Z is the effective impedance of the speaker coil. Furthermore, by inferring that our setup can be modeled as an ideal jet propulsion system and a regular electric system, we can expect a correlation between the driving voltage and thrust as $V \propto T^{3/4}$. In Fig. 2b, we observe that the maximum thrust value of each curve to the ¾ power as a function of the driving voltage results in a noteworthy linear behavior. The dashed line is a guide to the eye where

Fig. 2. a) Thrust (T) as a function of the loudspeaker driving voltage frequency for 4 different driving voltage amplitudes of the loudspeaker: 0,46 V, 0,94 V, 1.39 V, 1,86 V. Nozzle exit diameter is D = 21 mm. b) Maximum thrust of each curve to the power of ¾, as a function of the driving voltage.
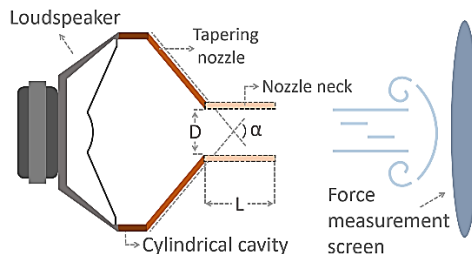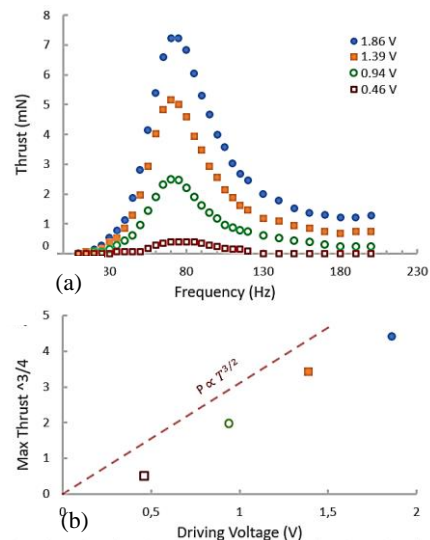
Fig. 1. Experimental setup for the production of acoustic jets. The sketch exhibits the following parameters: nozzle exit diameter (D), tapering angle (α) and nozzle neck length (L). In some measurements, a 5-cm-long cylindrical cavity was placed between the loudspeaker and the tapering nozzle.
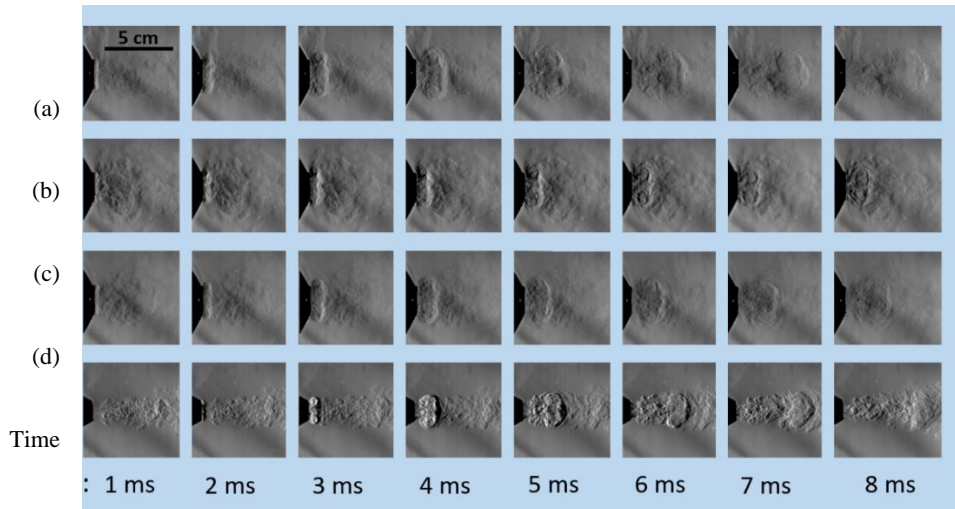
Fig. 3. Schlieren imaging of the jets acoustically produced in conditions with varying intensities, frequencies, tapering angle and nozzle exit diameter size: a) Driving voltage V = 1,86 V, frequency F = 100 Hz, tapering angle α= 120°, nozzle exit diameter D = 23,0 mm. b) V = 1,86 V, F = 50 Hz and α= 120°, D = 23,0 mm, c) V = 0,94 V, F = 100 Hz and α= 120°, D = 23,0 mm, d) V = 1,86 V, F = 100 Hz and α= 60°, D = 13,5 mm. Time interval between images is 1 ms as marked in the bottom row. In the supplementary materials, we provide an animated gif that evidences the vortex dynamics for each case.

the slope was adjusted to the experimental data. As discussed, the constant of proportionality depends on several parameters related to the intricate fluid dynamics of the experiment, since the physics of synthetic jets is distinct from traditional jet propulsion systems, and the intricacies that determine the yield of the loudspeaker, which may also account for the systematic shift of the data toward lower values of thrust. Thus, we must be cautious when considering the inset as a result *per se*. Nevertheless, the correlation is remarkable and indicates that the measurements are sound with the striking regular behavior of the four curves.

2.2 Schlieren Photography Measurements

A systematic Schlieren photography study was conducted using a Toepler system with two 300-mm-diameter mirrors, both with a 1500-mm focal distance and an optical surface quality of 40-20 scratch-dig. We used a 1.9-W, 425-nm LED illumination with a vertical knife edge filter. Images were acquired with a Fastec TX3 fast camera. For the sake of contrast improvement, the air inside the nozzle was heated with a 10-W resistor for 1 minute prior to every measurement. The study sustains that the measured propulsion is the result of synthetic jets produced by the loudspeaker.

In Fig. 3, we observe typical results that turn evident the vortex ring structures in different experimental conditions that are consistent with all experimental data in this work. The thrust force measurement system was not available at the Schlieren photography facility. However, with the acquired knowledge (and verifiable in Section 2.4), we can claim that the experimental conditions of Fig. 3a were close to the optimized thrust. By careful analysis of Schlieren images, we determined that the

propagation velocity of the ring structure in this condition was 7.2 m/s.

2.3 Theoretical and Numerical Considerations

Since the initial publications by Rogers (1858) and Helmholtz (1858), several studies and models on vortex rings have been performed, and their evolution in parallel with mathematical and computational tools over this period is remarkable. A classic view of the phenomenon is presented by Lamb (1993), who models the Stokes stream function of the vortex ring in cylindrical coordinates as

$$\psi(r,x) = \frac{\kappa}{2\pi}(r + R)[K(E(\lambda)) - E(\lambda)] \quad (5)$$

where r and R are the flow radius and ring radius of the vortex ring, respectively; κ is the vortex filament of strength or "circulation" in its constant half-plane; λ is the ratio

$$\lambda = \frac{R-r}{R+r} \quad (6)$$

and $K(\lambda)$ and $E(\lambda)$ are the complete elliptic integral of the first kind over λ and complete elliptic integral of the second kind, respectively. The vorticity is assumed to be a combination of the filament strength and the coordinates of the vortex filament, with the expression

$$\omega(r,x) = \kappa\delta(r - r')\delta(x - x') \quad (7)$$

with (r',x') as the cylindrical coordinates of the vortex filament. $\delta(x)$ is the Dirac delta function. This model of an ideal vortex ring establishes the boundary situation in which the rotating flux ring has

zero radius, and the ring is a circular line.

If we consider that the vortex ring has a thickness, the vortex ring can be approximated by a disk with a radius much smaller than the ring radius. Therefore, we have $r/R \ll 1$, which leads us to $1 - \lambda^2 \approx 4r/R$, and in the limit $r_1 \to 0$, $\lambda \to 1$. Under these conditions, the elliptical integrals have the following solution

$$K(\lambda) = \frac{1}{2} \ln \left(\frac{16}{1-\lambda^2} \right) \tag{8}$$

and

$$E(\lambda) = 1. \tag{9}$$

We can also consider the approximation of a uniform vorticity, which is formally $\omega(r,x) = \omega_0$, which leads us to a Stokes stream function given by

$$\psi(r,x) = \frac{\kappa \omega_0}{2\pi} R \iint \ln \left(\frac{8R}{r_1} - 2 \right) dr' dx' \tag{10}$$

whose most important results for our study are the circulation

$$\Gamma = \pi \omega_0 a^2, \tag{11}$$

Here, a is the radius of the disk, the hydrodynamic impulse is

$$I = \rho \pi \Gamma R^2 \tag{12}$$

and the kinetic energy is

$$E = \frac{1}{2} \rho \Gamma^2 R \ln \left(\frac{8R}{a} - \frac{7}{4} \right). \tag{13}$$

This thin-core vortex ring model enables us to estimate the translational velocity for the ring:

$$U = \frac{E}{2I} + \frac{3}{8\pi} \frac{\Gamma}{R}. \tag{14}$$

For the simulations, we solve the Navier–Stokes equations that are properly simplified for the problem, where we consider the fluid (air) as
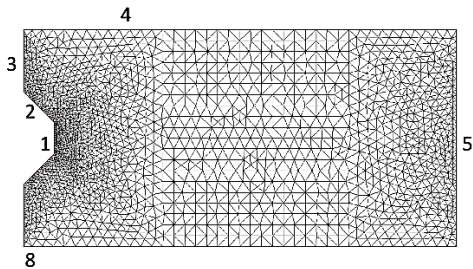

Fig. 4. Grid mesh of the simulations. Wall 1 is the source of the pulse with the velocity in the forward direction during a time interval. Walls 2 and 8 are solid walls, and all other boundaries present free conditions.

compressible, adiabatic and with its nonzero

viscosity. Integration over time was performed using the *FreeFem++* software (Hecht 2012), which was also used to generate the mesh, initial conditions and resulting data.

The simulations were performed considering the symmetries of the problem and the recommendations proposed by De Guyon and Mulleners (2021). The generated scene represents a 2D section that contains the main axis, which corresponds to the advance movement of the ring. The initial conditions are 1 atm and constant density throughout the environment with zero velocities. The only region different from these conditions is the speaker output, which is represented by a wall that has its velocity in the x direction changed by a time interval equivalent to one pulse to mimic the ring generation. Afterwards, the velocity on the wall becomes zero again. In Fig. 4, the details of the edges of the calculation scenario are presented with the grid mesh.

We consider an incompressible, isothermal Newtonian flow (density ρ =const, viscosity μ =const, no gravity) with a velocity field $\vec{v} = (u_r, u_\theta, u_Z)$ in its cylindrical form:

$$\frac{1}{r} \frac{\partial(ru_r)}{\partial r} + \frac{1}{r} \frac{\partial(u_\theta)}{\partial \theta} + \frac{\partial u_z}{\partial z} = 0 \tag{15}$$

$$\rho \left(\frac{\partial u_r}{\partial t} + u_r \frac{\partial u_r}{\partial r} + \frac{u_\theta}{r} \frac{\partial u_r}{\partial \theta} - \frac{u_\theta^2}{r} + u_z \frac{\partial u_r}{\partial z} \right) = -\frac{\partial P}{\partial r} \tag{16}$$

$$\rho \left(\frac{\partial u_\theta}{\partial t} + u_r \frac{\partial u_\theta}{\partial r} + \frac{u_\theta}{r} \frac{\partial u_\theta}{\partial \theta} - \frac{u_r u_\theta}{r} + u_z \frac{\partial u_\theta}{\partial z} \right) = -\frac{1}{r} \frac{\partial P}{\partial \theta} \tag{17}$$

$$\rho \left(\frac{\partial u_z}{\partial t} + u_r \frac{\partial u_z}{\partial r} + \frac{u_\theta}{r} \frac{\partial u_z}{\partial \theta} + u_z \frac{\partial u_z}{\partial z} \right) = -\frac{\partial P}{\partial z} \tag{18}$$

and

$$p = \rho \bar{R} \tau \tag{19}$$

where $\bar{R}$ is the ideal gas constant, and τ is the temperature.

Here, we present the most relevant results of the simulations. Fig. 5 shows the evolution of gas pressure and velocity at the same instants, i.e., t= 4, 6 and 8 ms. The instant $t_0 = 0$ is the moment when the pressure pulse at the loudspeaker output returns to zero. According to the simulations, the ring is immediately formed after t_0, which presents the nominal conditions expected from this phenomenon.

As the simulation progresses over time, two regions of low pressure accompany the ring: one ahead and the other behind. This is a natural consequence of the phenomenon's propagation, but it can be intuitively explained as the edges of the high-velocity region of the interior of the ring.

By introducing a normalized kinetic energy quantity, given by

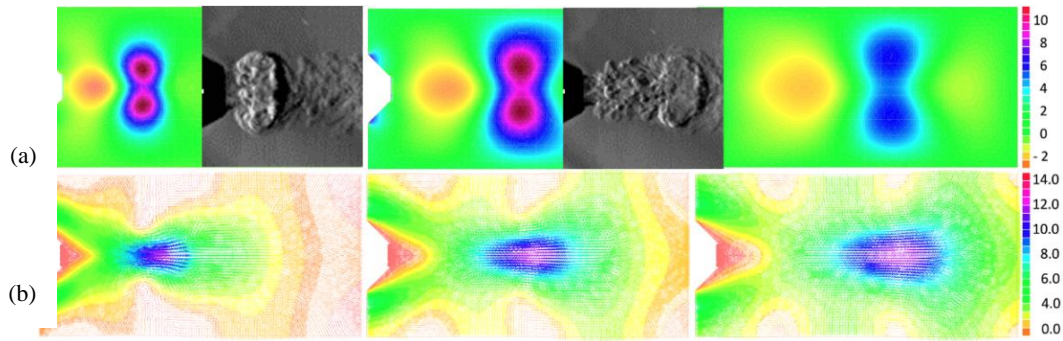$$E' = \frac{1}{2} \Gamma^2 R \ln \left(\frac{8R}{a} - \frac{7}{4} \right) \tag{20}$$

Fig. 5. Three moments of the simulation: t= 4, 6 and 8 ms from the beginning of the pulse, of the pressure and displacement of the ring. Line (a): the color represents the variation in pressure (in Pa) compared to normal pressure (1 atm) as indicated by the scale on the right of the last image. The first two images are compared with Schlieren photographs. Line (b): three moments of the simulation of the velocity in its vectorial form for the same instants of (a). The colored arrows and its length represent the variation in velocity (in m/s) in two dimensions compared to null movement.

one can estimate the point of best (or maximum) transport of energy. Fig. 6 presents the evolution of the ring radius, hydrodynamic impulse and normalized kinetic energy in the vortex ring. It is possible to distinguish an instant at t=0.94, which corresponds to the maximum kinetic energy. For subsequent times, the kinetic energy will quickly disappear, and the vortex ring is disaggregated.

In the experiments, the vortex rings are sequentially formed by the sinusoidal voltage input, and each following ring is slightly affected by the distribution of velocity and pressure left by the previous one. The low-pressure region ahead of the new ring binds to its counterpart in the preceding ring. As a final result, a "tube" is formed, which conducts the air flow and preserves the life of the rings for a longer time.

Meanwhile, for higher frequencies, a proper residence time for the air is not satisfied, and the close presence of a former ring can be disruptive to the stability of the next ring, as we show in the experimental results in the next sessions. However, under suitable conditions, we can use this "vortex ring driven tube" model to estimate the final numbers, which connect the simulations with the experiments.

Assuming the pulse diameter (region 1 of Fig. 4) as 23 mm and using the frequency of 100 Hz as a time base, we can denormalize the simulation results. As a result, a maximum pressure of 10 Pa was obtained in the circulating inner region of the ring (Fig. 5a).

Moreover, as seen in Fig. 5b, a vortex ring structure with a central axial velocity of 13 m/s embedded in stagnant surroundings is compatible with a 7.2-m/s propagation velocity of the vortex ring measured by Schlieren instrumentation. Under the hypothesis that the tube maintains its internal diameter constant throughout the experiment, this introduces us to a force of 10 mN applied to the bulkhead/sensor.

Based on the observations, vortex rings do not indefinitely propagate. In fact, three main phenomena result in a vortex ring: dissipation, self-induced instabilities, and space intervals between rings. The dissipation occurs due to the exchanges

of energy in infinitesimal packets between the ring and the environment. This energy loss occurs at the ring surface and is mainly linked to the viscosity of the medium. Its effect is to reduce circulation, which accelerates the generation of self-induced instabilities and destruction of the ring along the process. Self-induced instabilities were thoroughly formally and experimentally investigated by Windall and Sullivan (1973). These perturbations are characterized by resonant longitudinal oscillations that tend to increase in amplitude with the passage of time. The main result of these researchers is that the order of instability follows $ln(a/R)$ and tends to dissipate the ring when a/R approaches unity.

If the space between two rings is sufficiently small for there to be significant interference between the circulation of both, we will observe the self-destruction of the two rings. This is easy to understand: since the circulation is identical for all rings ("forward" on the inside and backward on the outside), the surface velocities of the fluid will have opposite directions at the point where the rings touch. This last form of dissipation gives us the ideal frequency for the experiments. If the frequency is too high, the rings get closer and destroy each other. If it is too low, the contribution to the formation of the "tube" with the airflow will be less effective.
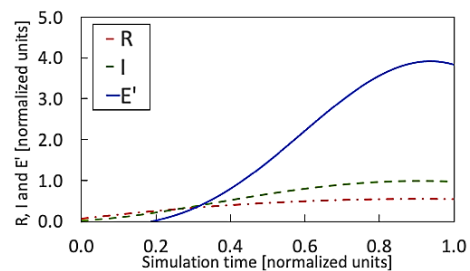

Fig. 6. Evolution of the ring radius, hydrodynamic impulse and normalized kinetic energy.

2.4 Relevant Parameters for Acoustic Jet Propulsion

In previous sections, we presented the behavior of the thrust generated by acoustic jets as a function of the amplitude and frequency of the applied voltage. Using Schlieren photography and simulations, we also established the nature of the jets as being composed of a sequence of vortex rings, which is consistent with the synthetic jet literature. In this session, we present experimental results for the behavior of the system's propulsion as a function of four other relevant parameters highlighted in Fig. 1: the nozzle neck length (L), nozzle exit diameter (D), tapering angle (α) and size of the system's internal cavity.

In Fig. 7, we show the behavior of the thrust as a function of the frequency of the driving voltage for several different nozzle neck lengths L. The fixed parameters were D = 18.4 mm and α = 60°, and the 5 cm long cylinder cavity was present in this series of measurements. We started with a nozzle neck length of 47 mm; prior to each measurement, we shortened the neck by 5 mm until it was totally removed. All curves present the same general trend observed in Fig. 2, i.e., an asymmetric curve with a peak of maximum thrust; however, the frequency position of this peak varies from $F = 55$ Hz to $F = 85$ Hz.

As shown in Fig. 7, although the length of the nozzle neck plays a secondary role in the resulting thrust at lower frequencies, it plays a major role in determining the frequency of the maximum thrust and its magnitude. Kordík and Trávníček (2018) and Gil and Smyk (2019) argued that the resonance frequency of the loudspeaker played a major role in the frequency of maximum thrust. However, the results in Fig. 7 indicate that the volume of air inside the cavity formed by the entire system loudspeaker plus nozzle also determines the overall frequency distribution of thrust. Paxton *et al.* (2007) obtained peak augmented thrust for considerably lower

(a)

(b)

Fig. 8. a) Behavior of the thrust as a function of frequency *F* (for a α = 60° and *V* = 1.86 V) for 9 different nozzle exit diameters D: 15.5, 17, 18.7, 29.5, 21.3, 24.5, 27,3, 29.5, 31.7 and 35 mm. The cylindrical cavity was absent and nozzle neck length L = 0 mm. The experimental data points of three significant curves are highlighted with symbols: D = 15,5 mm (open black circles), D = 24.5 mm (solid red circles) and D = 35 mm (open green squares). The data points of the other curves were suppressed for the sake of readability, since the behaviors are consistent. b) Excerpt from previous graph showing the behavior of the maximum thrust of each curve as a function of the nozzle exit diameter D.

frequencies (20 Hz), which is justified in their work in terms of a jet formation time parameter. However, since their work aimed to relate to conventional pulsejet propulsion, we believe that the configuration of their system considerably departs from the ideal synthetic jet propulsion design *per se* and relies on a large cavity and a long ejector. Thus, it can be argued that in addition to the dependency on the resonance frequency of the loudspeaker, the position of the maximum thrust also depends on the dampening effect of the volume of air encapsulated by the system. This also accounts for the low peak frequencies observed in the measurements of Fig. 1, where the cylindrical cavity was also present. For the next experimental results, the cylindrical cavity was removed, and no nozzle neck was present.

In Fig. 8a, we present the measurements of the thrust as a function of the frequency of the driving voltage (using V = 1.86 V) for 9 different nozzle exit diameters D. In all curves, the tapering angle was identical (α = 60°). For visualization, the experimental points are shown for three representative curves, i.e., for D = 15,5 mm (smallest nozzle exit diameter of the set), D = 24.5 mm (maximum yield) and D = 35 mm (largest diameter). All other curves are represented by lines, as the behavior of the thrust monotonically and consistently varies from one curve to another. The maximum
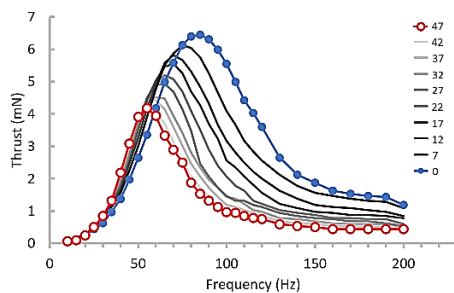
Fig. 7. Thrust as a function of the frequency of the driving voltage for 10 different nozzle neck lengths L from 0 to 47 mm in increments of 5 mm (except for the first step of 7 mm). Data points are shown only for L = 0 mm (closed blue circles) and L = 47 mm (open red circles). In all other experimental curves, the data points were suppressed for readability, since the behavior of the curves is consistent.
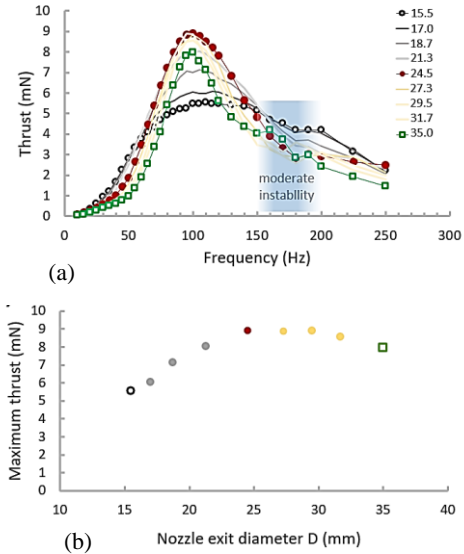
thrust frequency is approximately F = 100 Hz, which is considerably higher than that in Figs. 2 and 7. This fact corroborates our discussion regarding Fig. 7 in the sense that with no cylindrical cavity and nozzle neck, these later measurements were less influenced by the dampening effect of the air volume inside the system. Although it hardly affects the frequency of maximum thrust, the nozzle exit diameter D has a major influence on the overall distribution and maximum thrust magnitude. This result corroborates the low frequencies for thrust augmentation reported by Paxton *et al.* (2007), since their system aimed to relate to traditional pulse jet propulsion.

In the thrust measurements at 160-200 Hz, moderate instability was observed in the sense that the position of the screen to measure the force slightly swayed, so the measurement in that region was less precise, as can be sensed by the oscillation of the data points in this range of the graph. This effect was observed in all measurements, and as mentioned in Section 2.3, simulations indicate that this effect is related to the unsuitable residence time and couples with the thrust measurement screen. Interestingly, the instability of the screen diminished for frequencies above 200 Hz. However, one must consider that the thrust is also strongly mitigated in that range of frequencies.

In Fig. 8b, we depict the maximum thrust of each curve as a function of the corresponding nozzle exit diameter, which shows the consistent variation of the behavior of the curves, and the maximum thrust occurred for D = 24.5 mm (red closed circle).

The influence of the nozzle tapering angle (α) on the thrust can be examined in Fig. 9. In (a), we observe the behavior of the thrust as a function of the driving frequency for a fixed nozzle exit diameter D = 27,5 mm but for 4 different values of the tapering angle, i.e., α= 60°, 85°, 97° and 180°. The last value implies that instead of a cone-shaped nozzle, the loudspeaker was covered with a flat screen with a round orifice in the center (as in the first screen in Fig. 10). Interestingly, the tapering angle did not appear to significantly impact the thrust yield of the propulsion system, since all curves essentially overlapped and again had a thrust peak at approximately F = 100 Hz, as shown in Fig. 8. Importantly, the thrust measurement instability for F> 160 Hz was severe for α= 180° (the flat screen), which precluded measurements beyond 150 Hz. In Fig. 9b, we performed the same study in the inset of Fig. 8, i.e., the maximum thrust as a function of the nozzle exit diameter, but for 3 different tapering angles: α = 60°, 85° and 180°. Surprisingly, the largest trust was obtained for the flat screen and considerably larger exit diameters than other values of α. Arguably, nozzle engineering for propulsion systems seldom relies on flat obstructions to the flow, preferably on convergent and divergent sections. This result reveals how this study points to interesting new physics of jet propulsion.

To introduce the debate on nozzle engineering for synthetic jet propulsion, we devised an unconventional proposal in Fig. 10. The setup
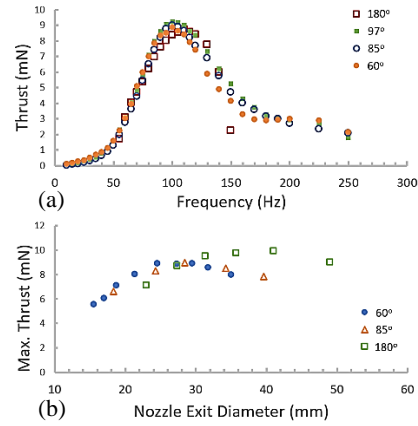

Fig. 9. a) Behavior of the thrust as a function of frequency for 4 different tapering angles: $\alpha = 60°$, $\alpha = 85°$, $\alpha = 97°$, $\alpha = 180°$. All measurements performed with the same exit diameter D = 27.5 mm without cylindrical cavity and nozzle neck. The driving voltage amplitude has been kept constant at V = 1.86 V. b) Identical to Fig. 8b but for three different tapering angles: α = 60°, α = 85° and α = 180°.

comprises a double-flat-screen structure. As the results of Fig. 9b show, the best thrust conditions are obtained for flat screens directly attached to the loudspeaker (without the cylindrical cavity) with a nozzle exit diameter D (orifice) of 30-45 mm. Thus, in our tests, a first flat screen with D = 33 mm was used (hereafter named D1 = 33 mm). A second flat screen with a varying orifice diameter D2 was placed at a varying distance "b" from the first screen, as indicated in Fig. 10.

A large portion of the kinetic energy of a synthetic jet is manifested in its rotational structure compared to its linear component. In this sense, the second screen acts by breaking the circulation component of the vortex ring and converting part of the circulation movement into an additional flow in the direction of the jet by letting the inner (forward) flow pass unobstructed and blocking the outer movement caused by the circulation.
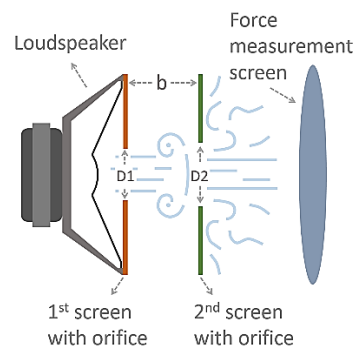

Fig. 10. Double-flat-screen setup for synthetic jet propulsion nozzle engineering.

Figure. 11 shows the results for thrust measurements as a function of the distance between the 1st and 2nd flat screen "b" for three different values of D2. For comparison, measurements in identical conditions but with the 2nd screen removed from the setup are shown. The results demonstrate that the proposal of Fig. 10 renders an improved thrust up to 20%. Moreover, although all three depicted 2nd screens showed improvements in thrust, the measurements indicate that the best results were obtained for D2 = 34 mm, which is very similar to D1 = 33 mm. The tests performed with D2 smaller than D1 did not improve the thrust. These results are not shown in Fig. 11 because they were obtained in distinct conditions; thus, it did not allow direct comparison. Furthermore, the measurements were strongly affected by the axial alignment of both screen orifices with respect to themselves and the direction of the jet flow. Thus, each datapoint is the average of 5 measurements. A relatable work has been performed by Kordík and Trávníček (2018) with a more constrained design and adherent results.

3. THERMOACOUSTIC JETS

In previous sections, we addressed the fundamental aspects of synthetic jet propulsion in air, and the employment of a loudspeaker has been justified as a functional device to produce suitable jets for the study. Moreover, as stated, current synthetic jet propulsion research is mostly aimed at underwater applications. This is also true for synthetic jets produced by a thermal cycle, as demonstrated by Piot (1892). In this section, we advance the last objective of this work, which is to demonstrate synthetic jet propulsion in air generated by a thermal cycle. This achievement is relevant for untethered applications of synthetic jets. We focused on 3 thermoacoustic mechanisms based on the tubular structures in Fig. 12. The first configuration is a tube open on both sides and widely known as a Rijke tube (Fig. 12a). It is often said that the Rijke tube operates only in a vertical position when standing still by using convection. However, when the hot and cold contrast
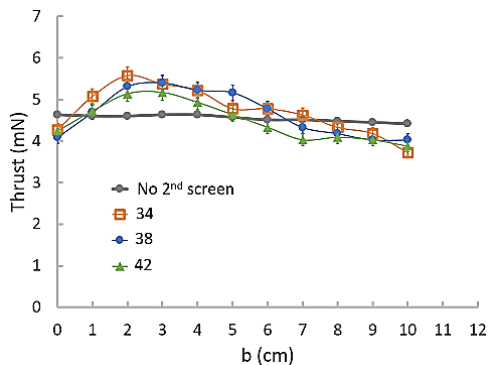
within the tube is well crafted, it also generates air flow in the horizontal position, as tested in our laboratory. The second configuration is known as the Sondhauss tube, and unlike a Rijke tube, it is closed at one end (Fig. 12b). Consequently, the acoustic behavior is changed, and the hot and cold contrast must be adjusted accordingly. The third tested configuration consists of a tube rigidly closed on one side and operates with a vibrating diaphragm on the other side (Fig. 12c). In this case, the acoustic resonance also depends on the elastic behavior of the diaphragm, which requires further adjustments to the resonance parameters. In this configuration, we expected to observe similarities with our acoustic results, since the diaphragm can be considered analogous to the loudspeaker's driving cone. In addition, a tapering nozzle has been attached, which mimics the acoustic mechanism described in previous sessions. In the three configurations, the resulting jet moved from left to right with respect to the drawing. We tested glass tubes of several sizes in all three configurations.

In all tests that we performed, configurations (a) and (c) resulted in perceptible but small thrust forces ($F < 0.5$ mN) that did not enable systematic characterization. Meanwhile, we obtained remarkable thrust values with the Sondhauss configuration (b) using a tube with a length of 95 cm and a diameter of 4.5 cm. We used a 600-W FeCrAl electric stove spring resistance as a heat source positioned 23 cm from the closed end. The cold section, which was positioned at approximately 28 cm from the closed end, maintained by a wet cloth on the outside, and associated with a steel mesh inside the tube for improved heat exchange. The experimental results (Fig. 13) show the thrust as a function of the heat power delivered to the joule resistance. The resonance regime was only obtained for powers above 200 W, where the thermoacoustic frequency was constant at 92 Hz. This value corresponds to a sound wavelength of $l = 373$ cm, which can be associated with the acoustic resonance of a 93,3-cm-long tube closed in one end, i.e., consistent with a nominal 95-cm glass tube. For powers levels above 200 W, we observe a monotonic increase in thermoacoustic thrust, which reached a maximum value of 2,7 mN at the maximum power of the joule heater (600 W).

Fig. 11. Thrust as a function of the distance between the 1st and 2nd flat screens "b" (see Fig. 10) for 3 different values of D2: 34 mm, 38 mm and 42 mm. The data in gray represent the thrust obtained in identical conditions, but without the 2nd flat screen. In all measurements V = 0.96 V, F = 75 Hz and D1 = 33 mm.
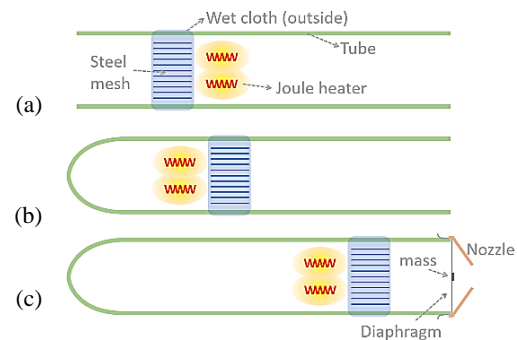

Fig. 12. Three tested configurations of thermoacoustic drivers for synthetic jets. (a) A horizontal Rijke tube. (b) A Sondhauss tube. (c) A vibrating diaphragm thermoacoustic engine.
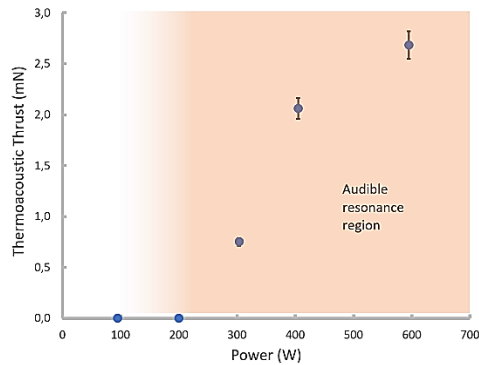
Fig. 13. Thermoacoustic thrust as a function of Joule heating power with a Sondhauss configuration (Fig. 12b).

4. CONCLUSIONS

Since current research on synthetic jet propulsion is essentially oriented to underwater applications, in this work, we demonstrated, characterized, modeled and simulated the propulsion generated by synthetic jets produced in air using a tapering nozzle directly attached to a compact 20-W loudspeaker, which yielded up to 10,4 mN of thrust. The results show consistent behavior of the thrust with respect to several relevant parameters such as the power, frequency, and geometric factors.

Since the pioneering work by Ingård and Labate (1950), several research papers have reported on the resulting force generated by synthetic jets while aiming for other applications. Insofar as the final objective of this work is propulsion, many new insights have been brought to attention. For example, while most authors focused on the electromechanical transducer response to the driving power while addressing the synthetic jet efficiency, our results indicate that the air volume encapsulated in the cavity of the system is a determinant of the performance of the synthetic jet propulsion system. Furthermore, important differences and similarities to traditional jet propulsion systems are discussed. We indicated a general similarity in the relationship between power and thrust. Meanwhile, while traditional nozzle engineering for jet propulsion often relies on convergent and divergent sections, our results demonstrate that the tapering angle of the nozzle plays a negligible role in the resulting jet propulsion, and the best results are obtained for a flat screen with an orifice directly attached to the loudspeaker. In addition, a nozzle engineering proposal based on an unconventional design comprising a double flat-screen setup with aligned orifices generated thrust up to 20% higher than the single-flat-screen configuration.

Finally, we demonstrated thermoacoustic jet propulsion, obtaining 2.7 mN of thrust using a 95 cm long and 4.5 cm diameter Sondhauss tube. Prior to this work, synthetic jet propulsion driven by thermal cycles was limited for liquid environments with the use of designs based on the patent by Piot (1892).

This work expands these applications to aerial environments.

AUTHORS' CONTRIBUTIONS

JS conceived the project, worked on the instrumentation, performed most of the experimental measurements and wrote the manuscript. DAM performed the Schlieren photography experiments. HF designed and constructed most of the instrumentation in the project. AHJ is responsible for the model and simulations in this work. FASM guided the project in the framework of propulsion, which provided theoretical assistance and literature input. All authors maintained close contact and communication during the project. All authors declare no conflicts of interest.

REFERENCES

Backhaus, S. and G. Swift (1999). A thermoacoustic stirling heat engine. *Nature* 399, 335–338.

Blade, A. (2021). *Thermoacoustic heat engine with thrust? - short heat engine experiment with standing wave* [Video], march 6th. https://youtu.be/uZwQwztWC2A. retrieved 24/08/21.

Chang, J., S. Zheng, Y. Du, J. Xu, Y. Liu, B. Guo, Y. Pan, B. Han (2020). Investigation of vortex rings for free jet and synthetic jet at various reynolds numbers and strouhal numbers. *Mathematical Problems in Engineering* Article ID 1503628.

Chen, G., G. Krishan, Y. Yang, L. Tang and B. Mace (2020). Numerical investigation of synthetic jets driven by thermoacoustic standing waves. *International Journal of Heat and Mass Transfer* 146,118859.

Chitsaz, I., M. H. Saidi, and A. A. Mozafari (2011). Semi analytical solution to transient start of weakly underexpanded turbulent jet. *Journal of fluids engineering* 133(9), 091204.

Crowther, W. J. and L. T. Gomes (2008) An evaluation of the mass and power scaling of synthetic jet actuator flow control technology for civil transport aircraft applications. *Proceedings of the Institution of Mechanical Engineers, Part I: Journal of Systems and Control Engineering* 222 (5), 357-372.

Dabiri, J. O. (2009). Optimal vortex formation as a

unifying principle in biological propulsion. *Annual Review of Fluid Mechanics* 41, 17–33.

De Guyon, G. and K. Mulleners (2022). Estimating the non-dimensional energy of vortex rings by modelling their roll-up. *Journal of Fluid Mechanics* 940.

Dobson, R. T. (2003). An open oscillatory heat pipe steam-powered boat. *International Journal of Mechanical Engineering Education* 31, 4 339-358.

Geng, T., F. Zheng, A. V. Kuznetsov, W. L. Roberts and D. E. Paxson (2010). Comparison between numerically simulated and experimentally measured flowfield quantities behind a pulsejet. *Flow Turbulence Combust* 84, 653-667.

Gil, P. and E. Smyk (2019). Synthetic jet actuator efficiency based on the reaction force measurement. *Sensors and Actuators A: Physical* 295, 405-413.

Glezer, A. and M. Amitay (2002). Synthetic jets. *Annual Review of Fluid Mechanics* 34, 503-529.

Hecht, F. (2012). New development in FreeFem++. *Journal of Numerical Mathematics* 20 (3-4), 251-266.

Helmholtz, H. V. (1858). Über integrale der hydrodynamischen gleichungen, welche den wirbelbewegungen entsprechen. *Journal für die Reine und Angewandte Mathematik* 55, 25-55.

Holman. R., Y. Utturkar, R. Mittal, B. L. Smith and L. Cattafesta (2005). Formation criterion for synthetic jets. *American Institute of Aeronautics and Astronautics Journal* 43(10), 2110-2116.

Ingård, U. and S. Labate (1950). Acoustic circulation effects and the nonlinear impedance of orifices. *The Journal of the Acoustical Society of America* 22(2), 211-218.

Ingård, U. (2008). *Notes on Acoustics*. Infinity Science Press, LLC, Hingham.

Ishii, R., H. Hujimoto, N. Hatta and Y. Umeda (1999). Experimental and numerical analysis of circular pulse jets. *Journal of Fluid Mechanics* 392, 129-153.

Jankee, G. K. and B. Ganapathisubramani (2019). Influence of internal orifice geometry on synthetic jet performance. *Experiments in Fluids* 60(4), 1-11.

Jeng, T. M. and W. T. Hsu (2016). Experimental study of mixed convection heat transfer on the heated plate with the circular-nozzle synthetic jet. *International Journal of Heat and Mass Transfer* 97, 559-568.

Kordík, J. and Z. Trávníček (2018) Novel nozzle shapes for synthetic jet actuators intended to enhance jet momentum flux. *Actuators* 7 (53), 1-13.

Lamb, H. (1993). *Hydrodynamics*. Cambridge University Press, New York.

Li, C. and J. Yang (2017) Roll control using only synthetic jet actuators at high angle of attack. *Journal of Aircraft* 54 (1), 369-375.

McCormick, D. C. (2000). Boundary layer separation with directed synthetic jets. In *American Institute of Aeronautics and Astronautics 38th Aerospace Sciences Meeting and Exhibit*, Reno, Nev USA.

Pack, L. G. and A. Seifert (2001). Periodic excitation for jet vectoring and enhanced spreading. *Journal of Aircraft* 38(3), 486-495.

Paxson, D. E., M. P. Wernet and W. T. John (2007). Experimental investigation of unsteady thrust augmentation using a speaker-driven jet. *AIAA Journal* 45 (3), 607-614.

Piot, T. (1892). Improvements in Steam Generators. UK Patent 20,081 Issue date: 0ct. 15.

Qin. L., Y. Xiang, S. Qin and H. Liu (2020). On the structures of compressible vortex rings generated by the compressible starting jet from converging and diverging nozzles. *Aerospace Science and Technology* 106, 106188.

Rogers, W. B. (1858). On the formation of rotating rings by air and liquids under certain conditions of discharge. *The American Journal of Science and Arts* 26, 246–258.

Swift, G. W. (1988). Thermoacoustic engines. *The Journal of the Acoustical Society of America* 84, 1145.

Thomas, A. P., M. Milano, M. G. G'Sell, K. Fischer and J. Burdick (2005). Synthetic jet propulsion for small underwater vehicles. *Proceedings of the 2005 Institute of Electrical and Electronics Engineers International Conference on Robotics and Automation*, IEEE.

Trávníček, Z., Z. Broučková and J. Kordík (2012). Formation criterion for axisymmetric synthetic jets at high stokes numbers. *American Institute of Aeronautics and Astronautics Journal* 50(9), 2012-2017.

Wang, H. and S. Menon (2001). Fuel–air mixing enhancement by synthetic microjets. *American Institute of Aeronautics and Astronautics Journal* 39(12), 2308-2319.

Windall, S. E. and J. P. Sullivan (1973). On the stability of vortex rings. *Proceedings of the Royal Society of London A* 332, 335-353

Whitehead, J. and I. Gursul (2006) Interaction of synthetic jet propulsion with airfoil aerodynamics at low reynolds numbers. *AIAA Journal* 44 (5), 1753-1766.

Xu, H., Y. He, K. L. Strobel, C. K. Gilmore, S. P. Kelley, C. C. Hennick, T. Sebastian, M. R. Woolston, D. J. Perreault and S. R. Barrett (2018). Flight of an aeroplane with solid-state propulsion. *Nature* 563(7732), 532-535.